Cronfa - Swansea University Open Access Repository

_____

This is an author produced version of a paper published in:
Nanoscale

_____

Cronfa URL for this paper:
http://cronfa.swan.ac.uk/Record/cronfa39341

_____

Paper:

_____

http://www.swansea.ac.uk/library/researchsupport/ris-support/

ARTICLE

Unravelling the nucleation mechanism of bimetallic nanoparticles with composition-tunable core-shell arrangement †

Ting-Wei Liao,[a] Anupam Yadav,[a] Kuo-Juei Hu,[a,b] Johan van der Tol,[a] Salvatore Cosentino,[a] Francesco D'Acapito,[c] Richard E. Palmer,[d] Cristina Lenardi,[e] Riccardo Ferrando,[f] Didier Grandjean[a*] and Peter Lievens[a]

The structure and atomic ordering of Au-Ag nanoparticles grown in the gas phase are determined by a combination of HAADF-STEM, XPS and Refl-XAFS techniques as a function of composition. It is shown consistently from all the techniques that an inversion of chemical ordering takes place by going from Au-rich to Ag-rich compositions, with the minority element always occupying the nanoparticle core, and the majority element enriching the shell. With the aid of DFT calculations, this composition-tunable chemical arrangement is rationalized in terms of a four-step growth process in which the very first stage of cluster nucleation plays a crucial role. The four-step growth mechanism is based on mechanisms of a general character, likely to be applicable to a variety of binary systems besides Au-Ag.

Introduction

To extend the range of properties of intermetallic nanomaterials and their performance, a detailed understanding of their structures and mechanisms behind their formation is needed. In particular, the influence of the very initial stage of nanoparticle nucleation, in which few atoms meet and form a small growing nucleus, has not yet been studied experimentally at the atomic level. An important issue, which arises in this context, is whether this initial nucleation stage can be decisive for determining the atomic arrangement of the resulting nanoparticles at the end of their growth process. Here, we consider the growth of Au_xAg_{1-x} bimetallic nanoparticles[1, 2] (BNPs) produced by cluster beam deposition (CBD), in which a binomial theorem composition analysis method is proposed to precisely determine and adjust the composition, for x from 0.1 to 0.9, prior to deposition. Combination of scanning transmission electron microscopy (STEM), X-ray photoelectron spectroscopy (XPS) and reflection X-ray absorption fine structure spectroscopy (Refl-XAFS) indicate that the resulting nanoparticles always have mixed cores and nearly pure shells, with the minority component always enriching the core but being scarce in the shell. This surprising inversion of chemical ordering depending on composition is explained by a four-step growth process of general character in which the very initial stage of the growth plays a major role. This explanation is supported both by mass spectrometry experiments and Density Functional Theory (DFT) calculations.

BNPs[1, 2] have long been a subject of intense study for their unique plasmonic,[3] catalytic,[4, 5] electronic and magnetic[6] properties distinct from those of the bulk materials and their monometallic counterparts. These properties not only depend on BNP size[7, 8] and composition[9, 10] but also on their structural organization at the atomic level.[10, 11] Spatial atomic distribution in BNPs plays a pivotal role in defining the geometric and electronic structure of their surface, which in turn determines their physicochemical properties.[12, 13] As a large variety of chemical arrangements,[1, 2] such as mixed alloy, core-shell, segregated subcluster, and onion-like, are possible for nanoalloys, it is essential to understand and control the molecular mechanisms of synthesis to produce BNPs with the desired structure.[14]

Although BNPs with relatively uniform size, composition, and atomic arrangements can nowadays be synthetized by various colloidal synthetic protocols,[15, 16] very little is known of the underlying particle growth mechanisms. Recently a clear impact of the nature of the pre-nucleation species in solution on the final BNPs composition and spatial arrangement was demonstrated.[17] However, due to the complexity of the growth process in solution,[18] uncovering the atomistic details of BNPs

a. *Laboratory of Solid-State Physics and Magnetism, KU Leuven, Celestijnenlaan 200D - Box 2414, 3001 Leuven, Belgium.*
b. *Nanoscale Physics Research Laboratory, School of Physics and Astronomy, University of Birmingham, Birmingham, B15 2TT, United Kingdom.*
c. *CNR-IOM-OGG c/o ESRF LISA CRG - The European Synchrotron CS 40220, 38043 Grenoble Cedex 9, France.*
d. *College of Engineering, Swansea University, Bay Campus, Fabian Way, Swansea SA1 8EN United Kingdom*
e. *CIMaINa and Physics Department, Università degli Studi di Milano,Via Celoria 16, 20133 Milano, Italy*
f. *Dipartimento di Chimica e Chimica Industriale dell'Università di Genova, IMEM/CNR, via Dodecaneso 31, 16146 Genova, Italy*

† Electronic supplementary information (ESI) available: The full RToF mass spectrum of the main production from CBD, diameter distribution taken from STEM, XPS spectra of O 1s, Ag 3d and Au 4f, k^3 weighted XAFS spectra, Ag K-edge XAFS refinements, height histograms measured by AFM, XANES spectra, mass spectra of small size clusters and RBS spectra of deposited Au_xAg_{1-x} BNPs. See DOI: 10.1039/x0xx00000x
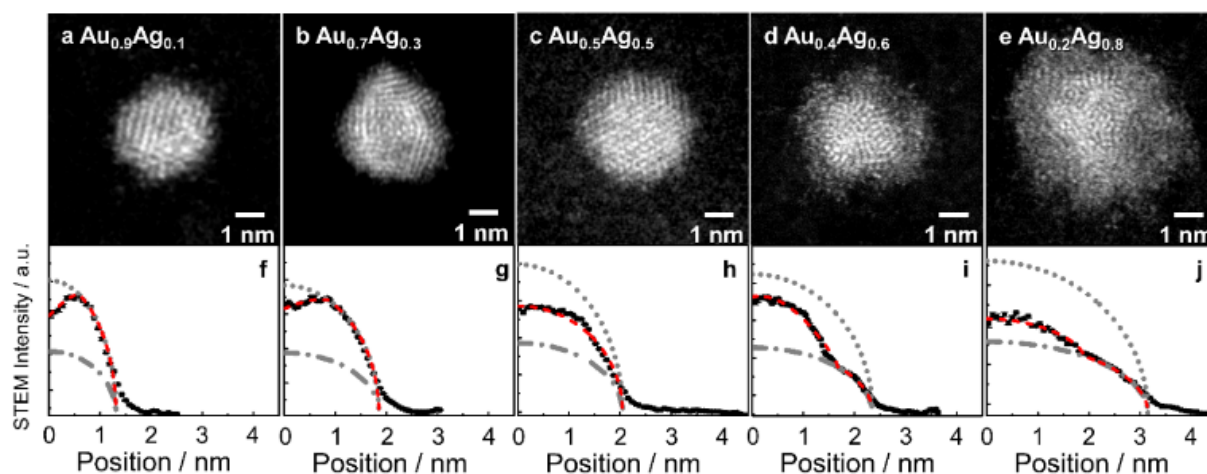
Figure 1. Example of detailed HAADF-STEM images of Au_xAg_{1-x} BNPs (top strip) with simulation results (bottom strip) also shown alongside: (a, f) $Au_{0.9}Ag_{0.1}$; (b, g) $Au_{0.7}Ag_{0.3}$; (c, h) $Au_{0.5}Ag_{0.5}$; (d, i) $Au_{0.4}Ag_{0.6}$; (e, j) $Au_{0.2}Ag_{0.8}$. The HAADF-STEM radial intensity profiles are taken from the centre to the edge of the cluster and integrated from 0° to 360°. The red dash lines are the simulations of cluster STEM intensity with gradient composition evolution. The grey dotted lines and grey dash dotted lines are simulated STEM intensities with pure Au clusters and pure Ag clusters, respectively. Additional STEM images of Au_xAg_{1-x} BNPs with larger and smaller sizes showing similar segregated structure are presented in Figure S2

growth processes experimentally is still difficult[17, 19] and theoretical models are rare.[20, 21] Experimental structural characterization of the (pre)nuclei and seeds formed during the nucleation process as well as of the final BNPs indeed remains a very challenging task.

To uncover the role composition plays on the final particle architecture we have used a new synthesis approach allowing the production of BNPs free of surfactant with a precise control of composition and of nucleation and growth processes. CBD indeed greatly benefits from producing clusters in a well-controlled noble gas environment and then soft landing them on supports while maintaining their preformed structure with excellent control over size and shape due to structural stability of the species present during the (pre)nucleation and growth stages in the gas phase.[22, 23] Moreover, the CBD setup is equipped with RToF-MS that allows a very fine control over the composition (see experimental methods).

Among the large number of bimetallic systems Au-Ag[24, 25] is widely studied for its full miscibility[26] and its unique optical[3] and catalytic[4, 5] properties. The excellent plasmonic properties of Au NPs[27] can be further enhanced and tuned as a function of composition through alloying with Ag.[10, 15] Enhanced catalytic activity and selectivity due to the synergistic effect of combining gold and silver has been reported.[10, 28, 29] Plasmon-mediated catalysis[30, 31] shows a clear "volcano type" relationship between chemical composition and catalytic activity of Au-Ag BNPs.[32] Finally Au-Ag BNPs are increasingly prominent in biomedicine[33] due to their photothermal properties,[34] combined with the antibacterial properties of silver[35] and the easy functionalization of gold.[36] This suggests that a precise control over their composition and atomic arrangement could allow a fine-tuning of Au-Ag BNP properties.

Due to identical lattice constants for Au and Ag,[37] direct lattice imaging of Au-Ag BNPs using TEM is not very informative and experimental reports on quantitative surface enrichment

are rare.[38, 39] Element selective HAADF-STEM, XPS and XAFS spectroscopies have proven to be the most appropriate techniques to characterize with high accuracy the structure of Au-Ag BNPs.[38, 40, 41] In parallel, the stable atomic arrangements of the final BNPs have been extensively modelled theoretically[42] with unclear and sometimes contradictory results while no studies have been reported on their nucleation and growth processes.

In this work we use the build-in RToF-MS to determine the composition of the deposited BNPs with high precision using a method based on the binomial combination theorem. By using a combination of HAADF-STEM, XPS and Refl-XAFS, the tunable spatial architecture and the interatomic charge transfer in the final Au-Ag BNPs as a function of composition is unravelled. The role of the nucleation stage in controlling this final spatial architecture of the BNPs is highlighted with the aid of DFT-based theoretical calculations and a four-step growth process is proposed.

Results and Discussion

A series of Au_xAg_{1-x} clusters from gold rich to silver rich stoichiometries were produced in the gas-phase by dual-laser ablation of pure Ag and Au metal targets and condensation in high pressure (~9 bar) helium gas.[43] The clusters were carried out of the source by the helium pulse at supersonic speeds and the formed beam is directed into the extraction region of the RToF-MS, where the clusters are photoionized with an excimer laser. The obtained mass spectrum was used to determine with high precision the cluster sizes and compositions present in the chamber at the end of the nucleation / growth process (Figure S1). The precise required composition of Au-Ag clusters was obtained by modulating the laser intensities ablating the two targets independently to produce $Au_{0.9}Ag_{0.1}$, $Au_{0.7}Ag_{0.3}$, $Au_{0.5}Ag_{0.5}$, $Au_{0.4}Ag_{0.6}$, $Au_{0.3}Ag_{0.7}$, $Au_{0.2}Ag_{0.8}$, and $Au_{0.1}Ag_{0.9}$ by a

composition analysis of the ultra-small cluster region of the mass spectra based on the binomial theorem (see experimental methods).

To unravel the atomic arrangements of Au and Ag atoms in Au-Ag BNPs as a function of their composition, gas-phase Au_xAg_{x-1} clusters (x = 0.2, 0.4, 0.5, 0.7 and 0.9) were deposited directly on TEM grids to yield random arrays of Au-Ag BNPs. They were investigated by STEM-HAADF whose signal brightness is directly related to the elemental atomic number Z. Due to the large Z difference between Au (79) an Ag (47) a strong contrast between brighter gold-rich and darker silver-rich areas is expected in the STEM images.

The average diameter of the BNPs measured for more than 100 NPs was 3.0 ± 0.7 nm in Au rich BNPs and 3.4 ± 0.7 (3.7 ± 0.8) nm in Ag rich $Au_{0.4}Ag_{0.6}$ ($Au_{0.2}Ag_{0.8}$). Histograms of diameter distributions of Au_xAg_{1-x} BNPs (Figure S3) show a sharp increase of the BNP diameter in silver-rich compositions due to their flattening on the support (see below).

Figure 1 presents STEM images of Au-Ag BNPs along with their normalised quantitative radial intensity profile integrated over the polar coordinate and simulated STEM radial profiles corresponding to pure Au NPs, pure Ag NPs and phase segregated structures. Detailed inspection of the STEM images shows that for all compositions except $Au_{0.5}Ag_{0.5}$ a contrasted dark core / bright shell or bright core / dark shell pattern is observed, while for the case of $Au_{0.5}Ag_{0.5}$, a uniform intermediate intensity prevails over the whole cluster. This indicates different levels of mixing and atomic arrangements are occurring in the deposited clusters as a function of their composition.

For gold rich BNPs the core appears darker than the shell, while for silver rich ones the reverse is observed showing a composition-tunable atomic arrangement. This is corroborated by the STEM profiles of the BNP cores that lie systematically between the simulated profiles of pure gold and pure silver indicating that the composition of the cluster core is always enriched by the minority element, i.e. silver in gold rich BNPs (x = 0.9 and 0.7) and gold in silver rich clusters (x = 0.4 and 0.2).

Detailed information on the composition variation along the radius of each BNP was obtained by simulating[44] the STEM signal intensity with different Au-Ag compositions from the centre to the edge of the BNPs. The obtained results are presented in Figures 1f to 1j and indicated with red dash lines. In all the investigated BNPs, except in $Au_{0.5}Ag_{0.5}$, the core composition varies as a function of the position along the BNP radius. In gold rich $Au_{0.9}Ag_{0.1}$ the centre of the cluster is composed of ca. 95% of Ag and the silver concentration decreases along the radius to reach 0% at a distance of 0.7 nm from the BNP centre. On the other hand, in silver rich $Au_{0.2}Ag_{0.8}$, the centre core is composed of ca. 90% Au and the Au concentration reaches 0% at 1.8 nm from the BNP centre.

The predominant location of Ag at the surface of the BNP in silver-rich compositions is further confirmed by the presence of an amorphous and highly dispersed phase around the NP metallic core in the STEM images of $Au_{0.2}Ag_{0.8}$ and to a lesser extent of $Au_{0.4}Ag_{0.6}$ BNPs (see Figures 1i and 1j). The absence of this phase in gold-rich BNPs is likely due to the presence of a

majority of gold atoms at the surface of the BNPs, forming sharp atomic planes and edges observed in the STEM images. This is also in line with the BNP size analysis shown in Figure S3, where an increase in the apparent average diameter in $Au_{0.2}Ag_{0.8}$ is observed, likely due to the presence of this amorphous oxide outer shell.

Detailed analysis of the STEM-HAADF images clearly shows the presence of a stable composition-tunable spatially segregated atomic arrangement in ca. 3 nm bimetallic Au_xAg_{1-x} with the minority element always preferentially located in the core of the particle. When the two elements are in equal amounts a full mixing of Au and Ag is observed.

Additional information on the composition-tunable arrangement and the charge transfers occurring between Ag and Au atoms in Au_xAg_{1-x} (x = 0, 0.1, 0.3, 0.5, 0.7, 0.9 and 1) BNPs was obtained by XPS. Ag 3d and Au 4f split due to spin-orbit coupling into Ag $3d_{3/2}$, Ag $3d_{5/2}$, Au $4f_{5/2}$ and Au $4f_{7/2}$ peaks, respectively, and O 1s spectra with best fits are presented in Figure S4. Analysis of O 1s peaks shows that the main signal is from the SiO_2 support and a contribution of Ag oxide (AgO ca. 530 eV, Ag_2O ca. 529 eV) is only present in Ag rich BNPs (x=0 and 0.1) with a contribution never exceeding 1% of the total O 1s peak. Analysis of the binding energies (BE) peak positions of Au $4f_{5/2}$, Au $4f_{7/2}$, Ag $3d_{3/2}$ and Ag $3d_{5/2}$ as a function of composition (Figure S4) show that Ag 3d BE in all Au_xAg_{1-x} BNPs are always smaller than that of pure Ag NPs. As the Ag BE decreases with increasing oxidation state due to its core-level photoemission,[45, 46] this evolution points out a systematic partial electron transfer from Ag to Au atoms or to the SiO_2 support in all BNPs. This is further confirmed by the BEs of the Au 4f contribution showing the reduction of Au atoms by Ag in Au rich BNPs and their oxidation by electron transfer to the support through the silver outer shell in their Ag rich counterparts, as reported previously [47-49]
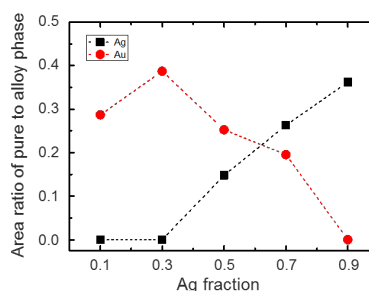
Figure 2. Integrated peak area ratio of the XPS Ag(0), pure phase, to Ag(δ), alloy phase, (black square) plotted with those of the Au(0), pure phase, to Au(δ), alloy phase, (red circle) from Au rich to Ag rich BNPs compositions.

The respective fractions of pure Au, pure Ag and Au-Ag alloyed phases present in all BNPs were examined by deconvoluting and fitting the Ag 3d and Au 4f peaks with two Ag and Au chemical components assigned to pure-phase Ag(0) and Au(0) peaks and an Au-Ag alloyed phase (Ag(δ) and Au(δ) peaks). The integrated peak area ratio of Ag(0) (368.5 eV and 374.5 eV) and Ag(δ) contributions (368.0 eV and 374.0 eV) in Ag 3d spectra and those of Au(0) (84.3 eV and 87.9 eV) and Au(δ)

(83.7 eV to 84.6 eV and 87.3 eV to 88.3 eV) in Au 4f spectra, respectively, are presented in Figure 2. The results indicate that the minority element always tends to form an alloyed phase while a large fraction (up to 40%) of the majority element forms a pure phase.

To further characterize the BNPs atomic arrangement, identify the different phases, and quantify the exact levels of mixing and segregation corresponding to the dark and bright regions in the final Au-Ag BNPs, we carried out a XAFS investigation of $Au_{0.9}Ag_{0.1}$, $Au_{0.7}Ag_{0.3}$, $Au_{0.5}Ag_{0.5}$, $Au_{0.3}Ag_{0.7}$, and $Au_{0.1}Ag_{0.9}$ clusters deposited on inert SiO_2 at the Ag K-edge. Unlike XRD and conventional TEM, XAFS can detect alloying in a few-atom size Au-Ag bimetallic system and even when the interatomic distances of the alloy and the pure metal are very similar.[40] The interference between Ag and Au phase shifts indeed generates a characteristic beat in the XAFS that appears as a doublet in the Fourier transform.[40] Moreover, analysis of the X-ray Absorption Near-edge Structure (XANES) can provide valuable information on the electronic properties of the BNPs and in particular on the electron transfer that is likely to occur between Au and Ag atoms.[50] The XAFS technique is also complementary to electron microscopy since it allows, as a bulk technique, the investigation of a more representative amount of clusters. However, to ensure that the BNPs always stay isolated on the SiO_2 support their coverage was kept to a very low value of 0.3 ML corresponding to an average inter BNP separation of around 7 nm. Due to this exceptionally high level of dilution the XAFS signal of the Au-Ag BNPs was collected in total reflection mode. Although the relatively weak signal that was collected for this exceptionally high level of dilution (0.3 ML) produced a moderate signal-to-noise ratio, a reliable XAFS signal still could be obtained up to k = 9.5 Å^{-1}. Phase corrected Fourier Transforms (Figure 3a) of the k^3-weighted XAFS (figure S5) show a doublet between 2 and 3 Å that is characteristic of Au-Ag alloys with distinct shape and intensity ratios for each compound, evidencing that a significant level of Au-Ag atomic mixing exists in most of the investigated compositions.

Detailed fitting of the data was carried out with a 3-shell structure model based on Ag-Ag, Ag-Au, and Ag-O interactions. In general, the major part of the XAFS signal could be fitted with a combination of Ag-Ag and Ag-Au contributions with Ag-Au and Ag-Ag contributions dominating in gold-rich and silver-rich compositions, respectively. Metallic coordination numbers (N_{Ag-Ag} and N_{Ag-Au}), obtained for these sizes in the spherical shape approximation, were generally smaller than expected, in particular in silver rich BNPs (see table S1). This may indicate that BNPs have a significant level of segregation with a pure Au region in line with the XPS results and/or that the Au-Ag BNPs are rather disordered and/or flattened onto the support in line with AFM images that show a significant flattening of the Ag rich BNPs on the SiO_2 surface compared to their Au-rich counterparts (Figure S6). This is likely resulting from the formation of a superficial oxide phase whose presence is evidenced by the minor Ag-O contributions detected mostly in Ag-rich BNPs with XPS. As Ag-O long bond distances (R_{Ag-O} = 2.24 to 2.20 Å) do not match those found in Ag_2O nor in AgO (2.04 Å),[37] this oxide likely corresponds to an amorphous phase

resulting from the interaction with the SiO_2 support of the large fraction of surface Ag atoms in absence of ligands. In silver rich $Au_{0.1}Ag_{0.9}$ this O contribution was 3 times stronger than in the other BNPs compositions, while Ag-O distances were shortened. This points out the formation of ca. 60% (N_{Ag-O} = 1.2 /N_{Ag-O} in Ag_2O or Ag/Si oxides[37] = 2) of an highly dispersed Ag oxide phase at the BNP/support interface. This is also visible in the STEM-HAADF image of $Au_{0.2}Ag_{0.8}$ and to a lesser extent of $Au_{0.4}Ag_{0.6}$. In gold-rich BNPs a limited amount of Ag oxide is found confirming the preferential location of silver in the BNP core where it is protected from oxidation by an outer shell of more noble gold metal. This Au shell confers gold-rich BNPs the compact shapes and sharp surface edges observed with STEM.

The evolution of metal-metal bond distances R_{Ag-Ag} and R_{Ag-Au} in Au-Ag BNPs as a function of Ag fraction are presented in Figures 3b and 3c. Whereas R_{Ag-Au} is close to the bulk values of both metals (2.88 Å)[37] for all compositions, R_{Ag-Ag} is unusually long (2.91 Å) in gold-rich $Au_{0.9}Ag_{0.1}$, unusually short (2.83 Å) in silver-rich $Au_{0.1}Ag_{0.9}$, and close to the typical silver metal bulk value in $Au_{0.5}Ag_{0.5}$.[51] These strong variations of bond distances suggest that the silver rich metal phase, unlike the Au-Ag alloy, might be located in very different spatial locations in the BNP depending on the composition. In the core of $Au_{0.9}Ag_{0.1}$ the Ag-Ag bond distance is affected by charge transfer to the surrounding more electronegative Au atoms depleting their electron density and resulting in weaker and longer Ag-Ag bonds in line with the XPS results.
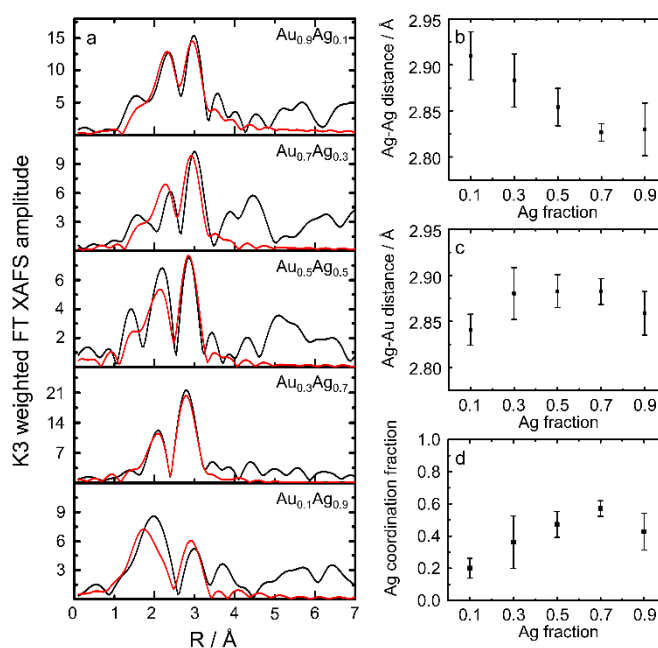
Figure 3. (a) Phase-corrected Fourier transformed XAFS spectra from gold rich to silver rich clusters. Bond distances of Ag-Ag (b) and Ag-Au (c), and Ag coordination fraction (Ag coordination number over the sum of Ag and Au coordination numbers) as a function of composition (d).

The charge transfer from Ag to Au atoms is indeed clearly visible in the XANES analysis of gold-rich $Au_{0.9}Ag_{0.1}$ and $Au_{0.7}Ag_{0.3}$ BNPs spectra presented in Figure S7. A strong white

line corresponding to the presence of a larger amount of empty states in the 5p band that is shifting the edge position to lower energies (25510.2 eV) compared to that of metal foil (25514.0 eV). In the meantime, both BNPs feature a strong resonance at 25545.2 eV characteristic of Ag metal, confirming that in both BNPs the large majority of Ag atoms does not form an oxide. In line with the Ag 3d XPS results, this XANES red-shift indicates the formation of electron-depleted alloyed metallic Ag due to their transfer to gold atoms. This charge transfer that is stronger in Au rich BNPs is likely stabilizing the Ag core against the galvanic replacement reaction, which explains the stability of this atomic arrangement.[47, 49] In contrast, in Ag-rich BNPs the nearly pure silver phase located in the outer shell of the BNP is likely undergoing a large surface tension that is shortening the Ag-Ag distances.[52, 53] The Ag coordination fraction number (ratio of Ag to the sum of Ag and Au coordination number) (Figure 3d) increases monotonically as expected with the Ag fraction in gold rich clusters and reaches a plateau in Ag rich compositions corresponding to the formation of an increasing amount of amorphous oxide phase.

Combining STEM-HAADF with XPS and XAFS spectroscopies allowed us to characterize the detailed atomic arrangements in Au-Ag BNPs deposited with CBD onto TEM carbon grids and SiO_2 wafers. Au-Ag BNPs are predominantly segregated with a composition-tunable inversion of the relative position of Ag and Au, *i.e.*, the less abundant element is always located in the core forming an alloy while the most abundant one is in the outer shell of the BNP with a significant fraction (up to 40%) forming a pure phase at the surface. Due to the lack of protecting ligands a limited fraction of the Ag atoms located at the BNP surface forms a dispersed amorphous oxide phase. Although two different supports were used for STEM and for XPS and Refl-XAFS spectroscopies, all techniques show for each composition similar structures. This suggests that the atomic arrangement of Au and Ag atoms in metallic BNPs is not significantly influenced by the deposition but may be determined at an earlier stage of the nucleation and growth stage occurring in the gas-phase before their deposition.

To test this hypothesis and better understand how the composition directly tunes the very different atomic arrangements observed in the final structures of Au-Ag BNPs we investigated the mechanism of Au and Ag atom mixing at the (pre)nucleation stage both theoretically using DFT and experimentally using RToF-MS. Although gas-phase cluster formation is believed to proceed *via* fast collision of hot vaporized metal atoms from the target with inert gas atoms, very little is known on the details of the nucleation and growth process.[54] It is generally accepted that the first step of the cluster growth comprises the formation of embryos[55, 56] consisting of ultra-small clusters of a few atoms[57] through three-body collisions. Upon embryo stabilization, the cluster may then further grow *via* cluster-cluster collision and/or atomic vapour condensation.[58]

While a limited amount of work on the formation of monometallic systems is available, no detailed bimetallic gas-phase cluster growth study has been reported to the best of our knowledge. To get more insight into the energy of formation of

Au-Ag bimetallic embryos we have evaluated their tendency to form mixed or pure clusters[59] by calculating the Au-Ag mixing energy in dimer, trimer, and tetramer clusters using spin-unrestricted density functional theory with the PBE functional (see methods).

Figure 4a shows that, in the case of tetramer clusters, the mixing energy of Au_2Ag_2 corresponds to a clear minimum. This value is 0.8 eV lower than for the monometallic clusters and implies that the formation of bimetallic Au_2Ag_2 clusters is energetically most favourable. Although this observation is made here specifically for four-atom clusters, this behaviour also applies to other small cluster nuclearities. It can also be generalized to other types of alloys since strongly negative mixing energy in small clusters have been reported in several bimetallic systems. These calculations concern miscible systems such as for example $PdCo$[60] and $AuPd$,[61] and even systems whose mixing energy is positive in the bulk, but not at the nanoscale, such as $AgCu$[62] and $AgNi$.[63] A consequence of this behaviour is that the relative abundance of the ultra-small bimetallic clusters present at the (pre)nucleation stage will always be higher than that of their monometallic counterparts.
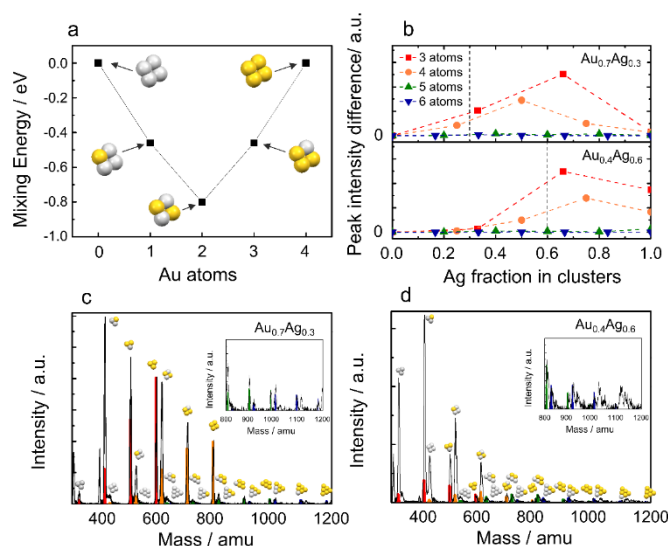
Figure 4. (a) DFT calculations of the mixing energy of tetramers: Ag_4, Au_1Ag_3, Au_2Ag_2, Au_3Ag_1, and Au_4. RToF-MS peak intensity difference of the relative abundance of trimers to hexamer, which are calculated from $Au_{0.4}Ag_{0.6}$ and $Au_{0.7}Ag_{0.3}$ RToF-MS. Vertical dash lines represent the global compositions and the 0 in y-axis corresponds to no abundance difference between the experimental and simulated MS (b). The corresponding RToF-MS of $Au_{0.7}Ag_{0.3}$ and $Au_{0.4}Ag_{0.6}$ with binomial combinatorial calculations of trimer (red), tetramers (orange), pentamer (green) and hexamer (blue) are shown in (c) and (d), respectively.

This hypothesis is nicely supported experimentally by the mass spectra collected during the gas-phase formation of $Au_{0.7}Ag_{0.3}$ and $Au_{0.4}Ag_{0.6}$ in the ultra-small cluster size range of less than 1200 amu. As the peak intensities are proportional to the clusters abundance, the excess abundance for each specific cluster composition is calculated by comparing the simulated peak intensities from the binomial combination theorem with the measured ones. RToF mass spectra peak intensities of Au_3, Au_4, Au_5, and Au_6 are taken as references, for the 3, 4, 5, and 6

atom clusters, respectively. The excess abundance for the 3, 4, 5, and 6 atom clusters during the nucleation of $Au_{0.4}Ag_{0.6}$ and $Au_{0.4}Ag_{0.6}$ BNPs are calculated by the peak intensity difference and plotted in Figure 4b, and the corresponding mass spectra are shown as Figures 4c and 4d. In the analysed size range from trimer to hexamer clusters forming during the $Au_{0.7}Ag_{0.3}$ and $Au_{0.4}Ag_{0.6}$ productions, the bimetallic trimers and tetramers are present in significant excess compared to the abundance expected for the binomial combination (Figure 4b). On the other hand, larger clusters nicely match the expected global composition indicating that the mixing energy is only playing a major role in the formation of the smallest clusters. Significant excess of pure Ag_3 and Ag_4 clusters observed in $Au_{0.4}Ag_{0.6}$ likely originates from the slight overstatement of the abundance of pure Ag clusters caused by the lower ionization of silver compared to gold.

Computational modelling in combination with experimental mass abundance spectrometry suggests that the Au-Ag mixing energy favouring the formation of ultra-small bimetallic clusters, dimers to tetramers, during the gas phase (pre)nucleation stage is responsible for the composition-tunable segregation behaviour of Ag and Au in the Au-Ag BNPs deposited on supports. Energetically favourable ultra-small bimetallic clusters are likely to form before their monometallic counterparts from the gas mixture of Au and Ag monomers present in the chamber during laser ablation and this process results in depleting the atoms of the minority element.[64] These small bimetallic clusters may then rapidly agglomerate by cluster-cluster collisions into larger nuclei keeping a similar average composition. These nuclei could form the core of BNPs that will appear systematically enriched with the minority element, except obviously for $Au_{0.5}Ag_{0.5}$. Monometallic clusters and /or atoms of the majority element aggregate later *via* cluster-cluster collision and atomic vapor condensation to form an outer shell enriched with the majority element. This process is in line with the formation of a partially segregated core-shell structure including a significant degree of alloying observed in the final structure of the Au-Ag BNPs.

Interestingly, similar processes have been reported for monometallic[65, 66] and bimetallic[17] gold-based NPs growth in solutions. For monometallic NPs, formation of small clusters from the Au monomers after partial reduction of the gold precursor was identified as the first step of the growth process. These clusters then formed seed particles with radii > 1.5nm attracting the remaining gold ions in two steps on top of the seed particles' surfaces until the precursor is fully consumed. In mixed-metal pre-nucleation of multinuclear metal-thiolate complexes, ultra-small tetramer bimetallic Au-Cu clusters were found to play a critical role in obtaining alloyed Au-Cu BNPs in solution, similar to the observations we here make for gas-phase growth in the laser ablation cluster source. Conversely, in two-phase syntheses, where these mixed metal-thiolate pre-nucleation species were absent, the formation of core-shell architectures was observed.[36]

DFT modelling supported by mass spectrometry suggests that, as for colloidal synthesis in solution, the chemical structure of the ultra-small clusters (less than 5 atoms) present in the gas-phase during the bimetallic cluster nucleation is likely tuning the final spatial atomic organization of the BNPs deposited onto supports. We propose a 4-step schematic representation of the growth process of Au-Ag clusters in the gas phase of a CBD source based on our combined investigation of the gas-phase nucleation stage and the post deposition BNPs final structures.
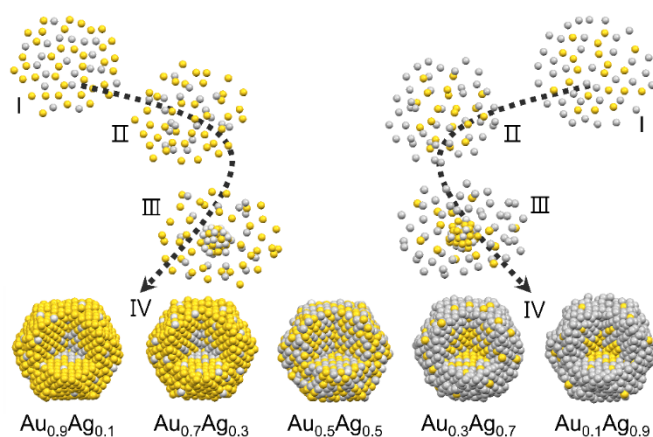
Figure 5. Schematic representation of the 4-step growth process of Au-Ag clusters in the gas-phase before deposition: (I) Au and Ag atoms are generated by laser ablation of the targets; (II) ultra-small bimetallic clusters form and the minority element is depleted from the metal gas; (III) the small bimetallic clusters serve as embryos or building blocks for the further growth of nuclei/seeds and the majority element atoms also condense on the bimetallic core to form the cluster shell; (IV) formation of clusters, with alloy cores enriched by the minority element and shell enriched by the majority element. A full alloy is formed in $Au_{0.5}Ag_{0.5}$.

As depicted in Figure 5, in the gas of monomers produced immediately after the laser ablation of two pure metal targets (I) the embryos or building blocks appearing in the monomers nucleation are bimetallic ultra-small clusters (up to 4 atoms) whose excess abundance is detected with mass spectrometry (II). In a second stage, these bimetallic clusters aggregate immediately into bimetallic nuclei/seeds that will form the alloyed core of the BNPs enriched in the minority element observed by STEM (III). The remaining part of the clusters or monomers enriched in the majority element that were formed later due to their less favourable mixing energy aggregate onto the preformed nuclei/seeds to form the pure and alloyed majority element outer shell of the BNPs (IV).

The proposed growth process may explain why the final atomic arrangement of Au-Ag BNPs presents a unique composition-tunable core-shell inversion with a systematic location of the minority and majority elements respectively in the alloyed core and in the rather pure outer shell of BNPs observed with STEM, XPS and Refl-XAFS. When the fraction of each element is equal, as in $Au_{0.5}Ag_{0.5}$, the (pre)nucleation mixed cluster composition reflects the global composition and remains constant during the whole growth process and no segregation is observed. This mechanism suggests that the final spatial atom architecture and the properties of Au-Ag BNPs may be tuned by controlling the composition of the cluster species present in the gas-phase prior to NP nucleation.

We believe that this may also apply to the synthesis of a large variety of bimetallic systems in the gas-phase but also in solution, since the main ingredient for obtaining this kind of behaviour is simply a strongly negative mixing energy for small clusters that also has been reported in other binary systems.[60-63, 67] This prospect may lead to major advances in the atom-scale control over multimetallic NP atomic arrangements and the surface atoms that are largely responsible for their catalytic and optical performance.

Conclusions

To uncover the role composition plays on the final particle architecture, Au-Ag BNPs of relatively uniform sizes, *ca.* 3 nm in diameter, and very precise compositions spanning the Au-Ag miscibility range were prepared by a new approach based on the CBD technology equipped with mass spectrometry enabling in-flight tuning of the cluster stoichiometry prior to deposition. Their combined structural characterization carried out by HAADF-STEM, XPS and Refl-XAFS, showed that both Au rich and Ag rich Au-Ag BNPs compositions are segregated with the minority element systematically predominant in the alloyed core of the BNP; the majority element is located in the outer shell with a significant fraction of pure phase. This composition-tunable core-shell arrangement is explained by the lower mixing energy of bimetallic ultra-small clusters that favours their formation over their pure counterparts in the early stage of the gas phase nucleation process. As favourable mixing energy of bimetallic ultra-small clusters is common to many bimetallic systems the proposed 4-step growth mechanism leading to composition-tunable chemical ordering inversion is likely applicable to other BNPs besides AuAg.

In summary, we showed that the overall compositions of the BNPs directly control their atomic arrangements. Precise control of the compositions of the nucleation species during the synthesis of BNPs may contribute further to designing novel BNPs with tailored atomic arrangements and their high performance properties for a wide range of applications.

Experimental Methods

Production of composition controlled clusters

Composition controlled Au-Ag bimetallic clusters are produced by pulsed laser (7 ns, 10 Hz, Nd:YAG lasers, Spectra Physics, INDI) ablation of Au (purity 99.995%) and Ag (purity 99.95%) or Au-Ag alloy (35 at% Au and 65 at% Ag, purity 99.95%) plate targets and inert gas (He, purity 99.9999%) condensation. The hot gas of metal monomers resulting from the pulsed laser ablation (100 µs) of the adequate metal targets confined in a small chamber undergoes aggregation upon cooling down in a 125 µs pulse of high-purity He (9 bar). The full mass spectrum (Figure S1) shows the production of a majority of large clusters and a small number of their small and ultra-small counterparts. Without mass selection, clusters are formed with sizes ranging from a few atoms to 1000 atoms.[68] In this study, the cluster production is optimized for clusters of about 1000 atoms. By

fine-tuning the laser power, the abundance of the two elements can be controlled and composition controlled bimetallic clusters are formed. The cluster source is cooled by liquid nitrogen, resulting in clusters with a temperature of about 100 K. After expansion into vacuum a molecular beam of clusters with different charge states is obtained, which is then soft-landed (~ 500 m/s) on an inert amorphous carbon film (~ 20 nm) covering a 200 mesh Cu TEM grid commercially available from EMS for STEM characterization or 5 cm long × 2 cm wide SiO$_2$ wafer in a UHV cluster beam deposition chamber with a base pressure below 5×10^{-10} mbar.[69] Most of the clusters (up to 90%) forming the cluster beam are neutral. The cluster beam size is 1 cm in diameter and the typical cluster flux is around 0.1 ML/min at the deposition stage 1 m downstream of the source. The dimension of the Refl-XAFS samples is 5 cm long × 2 cm wide, therefore, the depositions require movement of the sample stage to cover the 5 cm wafer, with a motorized 1 mm/s travel speed.

Reflectron time of flight mass spectrometry

Charged clusters formed directly in the source or neutral clusters are post-ionized by pulsed F$_2$ excimer laser (10 Hz, Lambda Physik OPTEX) photons (photon energy 7.9 eV, wavelength 157 nm), and are subsequently accelerated electrostatically and mass analysed by reflectron time-of-flight mass spectrometry with a mass resolution M/ΔM ≈ 150 at 591 amu and M/ΔM ≈ 250 at 1970 amu. A composition analysis method based on the binomial theorem analysis of the ultra-small cluster region of the mass spectra was developed to determine the composition of the Au-Ag clusters with high precision. With the direct proportionality of the intensity of each MS peak to the abundance of each type of bimetallic clusters and by assuming an identical ionization probability for clusters with the same number of atoms N, such as Au_N, $Au_{N-1}Ag_1$, $Au_{N-2}Ag_2$, $Au_{N-3}Ag_3$..., the intensity, $I_{Au_{N_{Au}}Ag_{N_{Ag}}}$ of the $Au_{N_{Au}}Ag_{N_{Ag}}$ cluster with N_{Au} number of Au atoms and N_{Ag} number of Ag atoms can be described by a binomial combinatorial relationship:

$$I_{Au_{N_{Au}}Ag_{N_{Ag}}} \propto \frac{(N_{Au}+N_{Ag})!}{N_{Au}!N_{Ag}!}[Au]^{N_{Au}}[Ag]^{N_{Ag}}, \qquad (1)$$

where $[Au]$ and $[Ag]$ are the normalized atomic fractions of Au and Ag elements, respectively.

Experimental RToF-MS spectra for each cluster composition were fitted to equation (1) using an in-house developed program to determine with high precision the global average composition of 5 to 15-atom ultra-small clusters. An example of the excellent match between the experimental and the simulated spectra corresponding to a global composition of 73.8 ± 0.4% Au and 26.2 ± 0.4% of Ag (Au$_{0.7}$Ag$_{0.3}$) is shown in Figure S8a.

Similarly simulation of the mass spectrum corresponding to clusters produced by laser ablation of an Au$_{0.4}$Ag$_{0.6}$ alloy target of defined composition (35.4% Au and 64.6% Ag, ACI alloy) (Figure S8b) shows that the simulated composition of Au$_{0.4}$Ag$_{0.6}$ (35.9 ± 0.7% Au and 64.1 ± 0.7% Ag), closely matches the original stoichiometry of the alloy targets supporting the validity of our approach.[23, 55] A very close composition (38% ±

4% Au and 62% ± 4% Ag) was also determined for the corresponding Au-Ag BNPs deposited on SiO_2 wafer by Rutherford backscattering spectrometry (RBS) (Figure S9) confirming the conservation of the composition of Au-Ag gas-phase clusters upon their soft landing as Au-Ag BNPs onto SiO_2 wafers.

Based on the developed method, the composition of bimetallic clusters can be monitored in real time by assuming a regular binomial distribution of the cluster compositions, and a series of simulated spectra from 0% to 100% of Ag with a 0.1% increment is made. The simulated spectra are then least-square-fitted to the measured mass spectrum, with the Au-Ag composition as the unknown fit parameter, using an in-house developed program. A validation of the fitting method applied on a series of mass spectra of Au_xAg_{1-x} is shown in Figure S10.

Rutherford backscattering spectroscopy

Rutherford backscattering spectroscopy experiments (Figure S9) were performed using a collimated mono-energetic He^+ beam accelerated by a dual Pelletron and steered into a scattering chamber. In this study, the 10 nA He^+ beam was focused to 2 mm^2 with kinetic energy in 1.57 MeV. The scattered He^+ beam was detected by a silicon surface barrier detector located at 15° to the surface normal.

Scanning transmission electron microscopy

Atomic resolution STEM imaging was performed by a JEOL JEM 2100F STEM instrument operating at 200 keV equipped with a spherical aberration (Cs) probe corrector (CEOS GmbH) and high-angle annular dark-field (HAADF) detector, with inner and outer collection angles of 62 and 164 mrad. The cluster size distribution of the Au-Ag BNPs were measured with low magnification images for more than 100 BNPs. The cluster size was determined by measuring the diameter cross-section of individual clusters. Assignment of core-shell structure was possible because of the Z-contrast of HAADF-STEM (Z is the elemental atomic number). The HAADF-STEM intensity is proportional to $Z^{1.46}$ with the camera length employed.[70] The large difference of the atomic number between Au and Ag (Z_{Au}=79; Z_{Ag}=47) allows us to distinguish the elemental atomic arrangement within the clusters directly from HAADF-STEM image intensity contrast. The STEM image analyzes were carried out with the imageJ Fiji software. The intensity profile of each single cluster was obtained by first finding the position of the centre through averaging, and then binning the intensity in polar coordinates as a function of the radial distance to the centre.

X-Ray Photoelectron Spectroscopy

XPS experiments were performed at room temperature under UHV condition (Leybold LHS 10/12, 5·10^{-9} mbar) by using Al Kα X-ray source operated at 10 kV and 25 mA and the spectra were collected by hemispherical analyser with passing energy 30 eV and energy step 0.025 eV. The spectra were aligned to the adventitious carbon peak C 1s placed at 284.8 eV. The fitting of the peaks was done with Unifit software. Following spin-orbit coupling constrains were considered: peaks separation 6.0 eV and 3.65 eV as well as peak area ratio 2/3 and 3/4 for Ag and Au, respectively.

X-ray absorption fine structure spectroscopy

XAFS experiments were performed in total reflection in fluorescence detection mode at Ag K-edge (25514 eV) on BM08-LISA beamline at The European Synchrotron (ESRF, Grenoble, France). 5 cm long × 2 cm wide SiO_2 ultra-flat wafers covered with 0.3 atomic monolayer (ML) clusters were mounted on a z-θ goniometer with the sample surface parallel to the ring orbital plane. The impinging beam was about 50 μm (v) × 2mm (h) and its intensity before and after the sample was collected with ion chambers filled with Ar gas. For each sample a reflectivity spectrum was collected and the data collection angle was defined as about 80% of the critical value for total external reflection. In this way the X-ray beam probes only a few nm below the surface enhancing the signal from the overlayer and minimizing that of the substrate.

The X-ray fluorescence yield from the Ag-$K_α$ line was collected using a multi-element HP-Ge detector array. Due to the limited fluorescent yield of Au L_3 edge that would have required excessive measurement times no data could be obtained at Au L_3 edge with this dilution.

Data reduction of the experimental X-ray absorption spectra was performed with the program EXBROOK.[71] Background subtraction and normalization was carried out by fitting (i) a linear polynomial to the pre-edge region in order to remove any instrumental background and absorption effects from other edges and (ii) cubic splines simulating the absorption coefficient from an isolated atom to the post-edge region. XAFS refinements were performed with the EXCURVE package.[71] Phase shifts and backscattering factors were calculated ab initio using Hedin-Lundqvist potentials. Fourier-transformation was applied to convert the k space spectra to r space with k^3 weighting to compensate for the dampening of the XAFS amplitude with increasing k. The structural models were built up with silver and surrounding atoms such as silver, gold and oxygen. The fitting results are presented in Table S1. The amplitude reduction due to many-electron processes (AFAC) was set to 0.9 after calibration with a silver metal foil.

Density Functional Theory

Spin unrestricted calculations were performed within the Density Functional Theory approach implemented in the Quantum-Espresso package[72] with available ultrasoft pseudopotentials.[73] For exchange and correlation, the spin unrestricted Generalized Gradient Approximation in the Perdew–Burke–Ernzerhof [74] implementation was used. For the selection of the plane waves, energy cutoffs of 40 and 160 Ry were chosen to describe the wave function and the electronic density, respectively. Convergence tests were made using cutoffs of 60 and 240 Ry. The mixing energy is defined here as the binding energy of mixed clusters with reference to the

binding energy of the corresponding monometallic clusters, and hence can be written as:

$$E_{mix(Au_mAg_n)} = E_{b(Au_mAg_n)} - \frac{m}{N}E_{b(Au_N)} - \frac{n}{N}E_{b(Ag_N)}, (2)$$

where E_b is the binding energy and $N = m + n$ is the total number of atoms. If $E_{mix(Au_mAg_n)} < 0$, the formation of a collection of N Au_mAg_n bimetallic clusters is energetically more favorable than that of a collection of m Au_N + n Ag_N monometallic clusters. By contrast, if $E_{mix(Au_mAg_n)} > 0$, the formation of a collection of monometallic clusters is energetically more favourable than that of their bimetallic counterparts.

Conflicts of interest

There are no conflicts to declare

Acknowledgements

References

1. R. Ferrando, J. Jellinek and R. L. Johnston, *Chem. Rev.*, 2008, **108**, 845-910.

2. R. L. Johnston and J. P. Wilcoxon, *Metal Nanoparticles and Nanoalloys*, Elsevier Science, 2012.

3. S. K. Cha, J. H. Mun, T. Chang, S. Y. Kim, J. Y. Kim, H. M. Jin, J. Y. Lee, J. Shin, K. H. Kim and S. O. Kim, *ACS Nano*, 2015, **9**, 5536-5543.

4. T. Benkó, A. Beck, K. Frey, D. F. Srankó, O. Geszti, G. Sáfrán, B. Maróti and Z. Schay, *Appl. Catal., A*, 2014, **479**, 103-111.

5. K. K. Haldar, S. Kundu and A. Patra, *ACS Appl. Mater. Interfaces*, 2014, **6**, 21946-21953.

6. S. H. Sun, C. B. Murray, D. Weller, L. Folks and A. Moser, *Science*, 2000, **287**, 1989-1992.

7. U. Kreibig and M. Vollmer, *Optical Properties of Metal Clusters*, Springer Berlin Heidelberg, 2013.

8. V. Habibpour, M. Y. Song, Z. W. Wang, J. Cookson, C. M. Brown, P. T. Bishop and R. E. Palmer, *J. Phys. Chem. C*, 2012, **116**, 26295-26299.

9. N. Jian and R. E. Palmer, *J. Phys. Chem. C*, 2015, **119**, 11114-11119.

10. J. F. Gomes, A. C. Garcia, C. Pires, E. B. Ferreira, R. Q. Albuquerque, G. Tremiliosi and L. H. S. Gasparotto, *J. Phys. Chem. C*, 2014, **118**, 28868-28875.

11. Y. Yang, J. Y. Liu, Z. W. Fu and D. Qin, *J. Am. Chem. Soc.*, 2014, **136**, 8153-8156.

12. M. J. Hartmann, H. Hakkinen, J. E. Millstone and D. S. Lambrecht, *J. Phys. Chem. C*, 2015, **119**, 8290-8298.

13. C. H. Cui, L. Gan, M. Heggen, S. Rudi and P. Strasser, *Nat. Mater.*, 2013, **12**, 765-771.

14. A. L. Gould, A. J. Logsdail and C. R. A. Catlow, *J. Phys. Chem. C*, 2015, **119**, 23685-23697.

15. K. D. Gilroy, A. Ruditskiy, H. C. Peng, D. Qin and Y. N. Xia, *Chem. Rev.*, 2016, **116**, 10414-10472.

16. R. G. Chaudhuri and S. Paria, *Chem. Rev.*, 2012, **112**, 2373-2433.

17. L. E. Marbella, D. M. Chevrier, P. D. Tancini, O. Shobayo, A. M. Smith, K. A. Johnston, C. M. Andolina, P. Zhang, G. Mpourmpakis and J. E. Millstone, *J. Am. Chem. Soc.*, 2015, **137**, 15852-15858.

18. E. E. Finney and R. G. Finke, *J. Colloid Interface Sci.*, 2008, **317**, 351-374.

19. X. L. Chen, J. Schroder, S. Hauschild, S. Rosenfeldt, M. Dulle and S. Forster, *Langmuir*, 2015, **31**, 11678-11691.

20. M. Wuithschick, S. Witte, F. Kettemann, K. Rademann and J. Polte, *Phys. Chem. Chem. Phys.*, 2015, **17**, 19895-19900.

21. F. D. Wang, V. N. Richards, S. P. Shields and W. E. Buhro, *Chem. Mater.*, 2014, **26**, 5-21.

22.V. N. Popok, I. Barke, E. E. B. Campbell and K. H. Meiwes-Broer, *Surf. Sci. Rep.*, 2011, **66**, 347-377.

23. B. Pauwels, G. Van Tendeloo, E. Zhurkin, M. Hou, G. Verschoren, L. T. Kuhn, W. Bouwen and P. Lievens, *Phys. Rev. B*, 2001, **63**, 165406.

24. Y. Herbani, T. Nakamura and S. Sato, *J. Phys. Chem. C*, 2011, **115**, 21592-21598.

25. H. Chen, R. Liu, L.-Y. Jang, J.-F. Lee and S. Hu, *Chem. Phys. Lett.*, 2006, **421**, 118-123.

26. S. Ristig, O. Prymak, K. Loza, M. Gocyla, W. Meyer-Zaika, M. Heggen, D. Raabe and M. Epple, *J. Mater. Chem. B*, 2015, **3**, 4654-4662.

27. T. W. Liao, S. W. Verbruggen, N. Claes, A. Yadav, D. Grandjean, S. Bals and P. Lievens, *Nanomaterials*, 2018, **8**, 30.

28. N. Sasirekha, P. Sangeetha and Y.-W. Chen, *J. Phys. Chem. C*, 2014, **118**, 15226-15233.

29. J.-H. Liu, A.-Q. Wang, Y.-S. Chi, H.-P. Lin and C.-Y. Mou, *J. Phys. Chem. B*, 2005, **109**, 40-43.

30. S. Sarina, H. Y. Zhu, Q. Xiao, E. Jaatinen, J. F. Jia, Y. M. Huang, Z. F. Zheng and H. S. Wu, *Angew. Chem., Int. Ed.*, 2014, **53**, 2935-2940.

31. Q. Xiao, S. Sarina, E. R. Waclawik, J. F. Jia, J. Chang, J. D. Riches, H. S. Wu, Z. F. Zheng and H. Y. Zhu, *ACS. Catal.*, 2016, **6**, 1744-1753.

32. J. L. Wang, R. A. Ando and P. H. C. Camargo, *ACS. Catal.*, 2014, **4**, 3815-3819.

33. W. J. Kim, S. Kim, A. R. Kim and D. J. Yoo, *Ind. Eng. Chem. Res.*, 2013, **52**, 7282-7288.

34. B. Hu, N. Wang, L. Han, M. L. Chen and J. H. Wang, *Acta Biomater.*, 2015, **11**, 511-519.

35. S. Chernousova and M. Epple, *Angew. Chem., Int. Ed.*, 2013, **52**, 1636-1653.

36. E. C. Dreaden, A. M. Alkilany, X. H. Huang, C. J. Murphy and M. A. El-Sayed, *Chem. Soc. Rev.*, 2012, **41**, 2740-2779.

37. M. Hellenbrandt, *Crystallogr. Rev.*, 2004, **10**, 17-22.

38. S. Hannemann, J. D. Grunwaldt, F. Krumeich, P. Kappen and A. Baiker, *Appl. Surf. Sci.*, 2006, **252**, 7862-7873.

39. Z. Y. Li, J. Yuan, Y. Chen, R. E. Palmer and J. P. Wilcoxon, *Appl. Phys. Lett.*, 2005, **87**, 243103.

40. I. J. Godfrey, A. J. Dent, I. P. Parkin, S. Maenosono and G. Sankar, *J. Phys. Chem. C*, 2017, **121**, 1957-1963.

41. R. J. Chimentao, I. Cota, A. Dafinov, F. Medina, J. E. Sueiras, J. L. G. de la Fuente, J. L. G. Fierro, Y. Cesteros and P. Salagre, *J. Mater. Res.*, 2006, **21**, 105-111.

42. C. M. Chang, C. Cheng and C. M. Wei, *J. Chem. Phys.*, 2008, **128**.

43. W. Bouwen, P. Thoen, F. Vanhoutte, S. Bouckaert, F. Despa, H. Weidele, R. E. Silverans and P. Lievens, *Rev. Sci. Instrum.*, 2000, **71**, 54-58.

44. Z. Li, J. Wilcoxon, F. Yin, Y. Chen, R. Palmer and R. Johnston, *Faraday Discuss.*, 2008, **138**, 363-373.

45. H. He, Y. Li, X. L. Zhang, Y. B. Yu and C. B. Zhang, *Appl Catal a-Gen*, 2010, **375**, 258-264.

46. H. Kannisto, H. H. Ingelsten and M. Skoglundh, *J Mol Catal a-Chem*, 2009, **302**, 86-96.

47. T. N. A. Dao, P. Singh, C. Shankar, D. Mott and S. Maenosono, *Appl. Phys. Lett.*, 2011, **99**.

48. T. Chen, S. Yang, J. S. Chai, Y. B. Song, J. Q. Fan, B. Rao, H. T. Sheng, H. Z. Yu and M. Z. Zhu, *Sci Adv*, 2017, **3**.

49. C. Shankar, A. T. N. Dao, P. Singh, K. Higashimine, D. M. Mott and S. Maenosono, *Nanotechnology*, 2012, **23**.

50. S. Nishimura, D. T. N. Anh, D. Mott, K. Ebitani and S. Maenosono, *Nanotechnology 2012, Vol 1: Advanced Materials, Cnts, Particles, Films and Composites*, 2012, 38-41.

51. J. T. Miller, A. J. Kropf, Y. Zha, J. R. Regalbuto, L. Delannoy, C. Louis, E. Bus and J. A. van Bokhoven, *J. Catal.*, 2006, **240**, 222-234.

52. Y. Sun, A. I. Frenkel, H. White, L. H. Zhang, Y. M. Zhu, H. P. Xu, J. C. Yang, T. Koga, V. Zaitsev, M. H. Rafailovich and J. C. Sokolov, *J. Phys. Chem. B*, 2006, **110**, 23022-23030.

53. W. J. Huang, R. Sun, J. Tao, L. D. Menard, R. G. Nuzzo and J. M. Zuo, *Nat. Mater.*, 2008, **7**, 308-313.

54. W. Knauer, *J. Appl. Phys.*, 1987, **62**, 841-851.

55. P. Milani and S. Iannotta, *Cluster beam synthesis of nanostructured materials*, Springer Science & Business Media, 2012.

56. A. I. Ayesh, N. Qamhieh, S. T. Mahmoud and H. Alawadhi, *J. Mater. Res.*, 2012, **27**, 2441-2446.

57. G. Scoles, D. Bassi and U. Buck, *Journal*, 1988.

58. T. Hihara and K. Sumiyama, *J. Appl. Phys.*, 1998, **84**, 5270-5276.

59. R. Ferrando, in *Frontiers of Nanoscience*, ed. F. Riccardo, Elsevier, 2016, vol. Volume 10, pp. 131-183.

60. M. Aslan, J. B. A. Davis and R. L. Johnston, *Phys. Chem. Chem. Phys.*, 2016, **18**, 6676-6682.

61. F. Pittaway, L. O. Paz-Borbon, R. L. Johnston, H. Arslan, R. Ferrando, C. Mottet, G. Barcaro and A. Fortunelli, *J. Phys. Chem. C*, 2009, **113**, 9141-9152.

62. M. Molayem, V. G. Grigoryan and M. Springborg, *J. Phys. Chem. C*, 2011, **115**, 22148-22162.

63. M. Molayem, V. G. Grigoryan and M. Springborg, *J. Phys. Chem. C*, 2011, **115**, 7179-7192.

64. K. Wegner, P. Piseri, H. V. Tafreshi and P. Milani, *J. Phys. D: Appl. Phys.*, 2006, **39**, R439-R459.

65. J. Polte, T. T. Ahner, F. Delissen, S. Sokolov, F. Emmerling, A. F. Thunemann and R. Kraehnert, *J. Am. Chem. Soc.*, 2010, **132**, 1296-1301.

66. J. Polte, R. Erler, A. F. Thunemann, S. Sokolov, T. T. Ahner, K. Rademann, F. Emmerling and R. Kraehnert, *ACS Nano*, 2010, **4**, 1076-1082.

67. S. Nunez and R. L. Johnston, *J. Phys. Chem. C*, 2010, **114**, 13255-13266.

68. Z. Li, H. Y. T. Chen, K. Schouteden, T. Picot, K. Houben, T. W. Liao, C. Van Haesendonck, G. Pacchioni, P. Lievens and E. Janssens, *Nano Lett.*, 2016, **16**, 3063-3070.

69. N. Vandamme, E. Janssens, F. Vanhoutte, P. Lievens and C. Van Haesendonck, *J. Phys.: Condens. Matter*, 2003, **15**, S2983-S2999.

70. Z. Wang and R. Palmer, 2012.

71. N. Binsted, J. Campbell, S. J. Gurman and P. C. Stephenson, *EXAFS analysis Programs; Daresbury Laboratory; Warrington, U.K.*, 1991.

72. P. Giannozzi, S. Baroni, N. Bonini, M. Calandra, R. Car, C. Cavazzoni, D. Ceresoli, G. L. Chiarotti, M. Cococcioni, I. Dabo, A. Dal Corso, S. de Gironcoli, S. Fabris, G. Fratesi, R. Gebauer, U. Gerstmann, C. Gougoussis, A. Kokalj, M. Lazzeri, L. Martin-Samos, N. Marzari, F. Mauri, R. Mazzarello, S. Paolini, A. Pasquarello, L. Paulatto, C. Sbraccia, S. Scandolo, G. Sclauzero, A. P. Seitsonen, A. Smogunov, P. Umari and R. M. Wentzcovitch, *J. Phys.: Condens. Matter*, 2009, **21**.

73. D. Vanderbilt, *Phys. Rev. B*, 1990, **41**, 7892-7895.

74. J. P. Perdew, K. Burke and M. Ernzerhof, *Phys. Rev. Lett.*, 1997, **78**, 1396-1396.